Document downloaded from:

http://hdl.handle.net/10251/202044

This paper must be cited as:

Mallón, L.; Cerezo-Navarrete, C.; Romero, N.; Puche Panadero, M.; García-Antón, J.; Bofill, R.; Philippot, K.... (2021). Ru nanoparticles supported on alginate-derived graphene as hybrid electrodes for the hydrogen evolution reaction. New Journal of Chemistry. 46(1):49-56. https://doi.org/10.1039/d1nj05215b

The final publication is available at

https://doi.org/10.1039/d1nj05215b

Copyright The Royal Society of Chemistry

Additional Information

Please do not adjust margins

ARTICLE

Ru nanoparticles supported on alginate-derived graphene as hybrid electrodes for the hydrogen evolution reaction

Received 00th January 20xx,
Accepted 00th January 20xx

DOI: 10.1039/x0xx00000x

Laura Mallón,[a,c] Christian Cerezo-Navarrete,[b] Nuria Romero,[a,+] Marta Puche,[b] Jordi García-Antón,[a] Roger Bofill,*[a] Karine Philippot,*[c] Avelino Corma,*[b] Luis M. Martínez-Prieto,*[b] and Xavier Sala*[a]

The development of organic-inorganic hybrid materials for redox catalysis is key to access new energy conversion schemes and the sustainable production of dihydrogen. Here on, bare and P-doped graphene arising from the pyrolysis of biomass (alginate from marine algae), have been used as a support for the growth and stabilization of ultra-small Ru/RuO_2 NPs through organometallic synthesis. P-doped graphene allows obtaining smaller and better dispersed NPs in hybrid electrodes of lower roughness and electroactive surface area. Electrochemical activation of the as-synthesised supported nanoparticles by reduction of the passivating RuO_2 layer generates excellent HER electrocatalysts under acidic conditions (η_{10} of 29 mV and 15 mV for the bare and P-doped electrodes, respectively). P doping, identified as surface phosphates by ^{31}P solid state NMR, induces improvement of all HER benchmarking parameters studied, including overpotential and exchange and specific current densities. All studied materials show excellent long-term stability and selectivity for hydrogen generation with no sign of deactivation after 12 h under turnover conditions and almost quantitative Faradaic efficiencies.

Introduction

The still massive consumption of fossil fuels triggers global warming through greenhouse gas (GHG) emissions and threatens both our lifestyle and the sustainability of our planet.[1] Thus, the development of renewable carbon-neutral fuels has become urgent and one of the pivotal societal challenges in the 21st century. In this regard, the renewable production of H_2 through water splitting (WS, $H_2O \rightarrow H_2 + ½O_2$) triggered by renewable energy sources (*e.g.* renewable electricity from sunlight or wind) is an appealing and clean alternative to steam reforming methods, which rely on fossil fuels and are intensive GHG emitters.[2] However, both WS half reactions, namely hydrogen and oxygen evolution reactions (HER and OER, respectively), occur through large activation energy barriers and, therefore, at high overpotentials. Thus, the development of highly active, sustainable and durable electrocatalysts, able to accelerate these reactions and lower the required overpotentials, is still a key challenge at the core of clean H_2 production from water.

Nanoparticles (NPs), with a high surface-to-volume ratio and tuneable surface properties, are interesting systems in (electro)catalysis and WS. In this respect, we have recently shown how the bottom-up synthesis of Ru NPs through the organometallic approach under mild conditions[3,4] allows obtaining ultra-small NPs with narrow size-distributions and controllable surface environments, which have a strong impact in their catalytic performance in both the HER[5,6,7] and the OER.[8,9]

The immobilization of NPs onto electrodes such as highly conductive carbon-based materials or oxides/metal oxides is a common way to improve (a) their long-term stability, preventing their agglomeration and sintering under catalytic conditions, and (b) their electron-transfer rates in practical electrodes. In this context, carbon-based (nano)materials (*i.e.* graphene) have shown to be excellent choices due to their high electrical conductivity and long-term stability together with a versatile morphology and rich surface chemistry.[10] Heteroatom-doping (*i.e.* N, S, P, O, *etc.*) of these carbon-based (nano)materials proved to be a powerful strategy not only to tune the physicochemical properties of the conductive supports themselves (*i.e.* electrical conductivity of the C-based nanomaterials) but also to influence the properties and affinity of the nanoparticles deposited at their surface.[11,6] The presence of doping heteroatoms thus influences either the activity, selectivity and long-term stability of the resulting hybrid electrocatalysts, and represents an interesting strategy to fine-tune their overall performance.[12]

[a.] *Departament de Química, Universitat Autònoma de Barcelona, Cerdanyola del Vallès, 08193 Barcelona, Spain, Roger.Bofill@uab.cat, Xavier.Sala@uab.cat*
[b.] *ITQ, Instituto de Tecnología Química, Universitat Politècnica de València (UPV), Av. de los Naranjos S/N, 46022 Valencia, Spain, luismiguel.martinez@csic.es, acorma@itq.upv.es*
[c.] *CNRS, LCC (Laboratoire de Chimie de Coordination), UPR8241, Université de Toulouse, UPS, INPT, F-31077 Toulouse cedex 4, France, Karine.Philippot@lcc-toulouse.fr*
[d.] *+. Actual address: CNRS, LCC (Laboratoire de Chimie de Coordination), UPR8241, Université de Toulouse, UPS, INPT, F-31077 Toulouse cedex 4, France.*
Electronic Supplementary Information (ESI) available: [details of any supplementary information available should be included here]. See DOI: 10.1039/x0xx00000x

Please do not adjust margins

Please do not adjust margins

With far higher surface area and charge carrier mobility than related graphitic materials,[13] graphene has emerged in recent years as a paradigmatic 2D carbon-support in electrocatalysis. However, practical application of graphene-based hybrid electrocatalysts relies on the development of scalable and sustainable methods to produce this carbon-nanomaterial. In this regard, graphene production through biomass carbonization, a waste-treatment technology, is an attractive method to reduce electrode costs and increase the sustainability of electrode production.[14]

Herein, we report the preparation of hybrid nanomaterials via the growth of ultra-small Ru NPs through organometallic synthesis on bare/P-doped graphene supports obtained from biomass (alginate from marine algae), and their evaluation as HER electrocatalysts under acidic conditions.

Results and Discussion

Synthesis and Characterization.

Biomass-derived bare and P-doped graphene supports (**G** and **P-G**, respectively) where prepared by pyrolysis of alginate and HPO_4^{2-}-modified alginate at 900 ºC, respectively, following reported methods.[15,16] Decomposition of the [Ru(COD)(COT)] (COD: cyclooctadiene and COT: cyclooctatriene) organometallic precursor under mild conditions (3 bar H_2, r.t, 20 h) in the presence of **G** or **P-G** supports, previously ultrasonicated in THF, yielded the graphene-supported Ru NPs (**Ru/G** and **Ru/P-G**) (Scheme 1).[17,18]

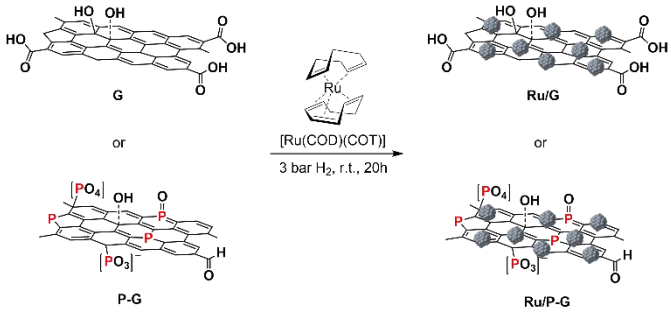

Scheme 1. Synthesis of **Ru/G** and **Ru/P-G** following the organometallic approach.

After an optimized digestion process (see Experimental Section), inductively coupled plasma atomic emission spectroscopy (ICP-AES) analysis showed a metal content of 2.6 wt.% and 3.3 wt.% for **Ru/G** and **Ru/P-G**, respectively. The two samples where then analysed by transition electron microscopy (TEM). As shown in Figure 1a-c, **Ru/P-G** revealed spherical, well distributed and monodispersed NPs with a mean diameter of 1.5 ± 0.3 nm. In contrast, the use of non-doped graphene (**G**) as a support yielded slightly larger (1.9 ± 0.6 nm) and more aggregated NPs (Figure 1, d-f). The difference in size and dispersion suggests that phosphorous atoms present in the P-doped graphene facilitate the formation and stabilization of smaller Ru NPs, as previously observed in similar N-doped graphene systems.[17,18] Figures 1 and S1 (see ESI†) also allow to infer the different exfoliation degree of the two supports (**G** and **P-G**). The presence of phosphate and sodium ions during the preparation of **P-G** seems to facilitate the separation of the carbon sheets, yielding a more exfoliated graphene support. The lower roughness of the **P-G** material (vs. **G**) has been later corroborated by electrochemical measurements (ECSA and RF, see Table 1 below).

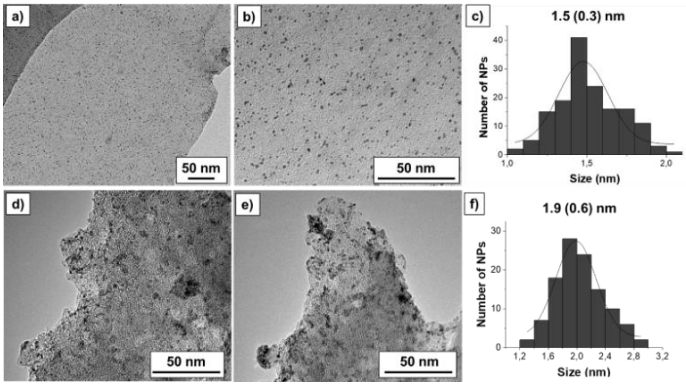

Figure 1. TEM images and size distribution histograms of Ru/P-G (a-c) and Ru/G (d-f).

High-resolution TEM (HRTEM) images and electron diffraction patterns confirmed the crystallinity of the Ru NPs in both **Ru/G** and **Ru/P-G**. From HRTEM micrograph of **Ru/P-G**, measurement of interplanar distances (see ESI†, Figure S2a) provided values of 0.21 and 0.23 nm, in agreement with the (002), (100) and (100) atomic planes of the hexagonal compact crystalline (hcp) structure of bulk ruthenium.

Raman spectroscopy was used to analyse and study the properties of graphene materials, both starting supports, as well as **Ru/G** and **Ru/P-G** catalysts. In all samples, two bands at *ca.* 1360 cm^{-1} (band D) and *ca.* 1600 cm^{-1} (band G) were observed, together with a broad peak centred at ca. 3000 cm^{-1} (band 2D'), which is related to a high exfoliation degree (see ESI†, Figures S3 and S4). The ratio of intensities of D and G bands (I_D/I_G) is a key parameter to determine the percentage of defects on graphene supports, which are excellent anchoring points for metal NPs, improving their stabilization.[19] As shown on Figures S3a and S4a), **P-G** presents a higher I_D/I_G ratio than **G** (2.39 for **G** and 2.81 for **P-G**), thus indicating the presence of more defect sites on the P-doped support. Moreover, the incorporation of Ru NPs on graphene supports led to a slight decrease in the two I_D/I_G ratios, indicating a higher sp^2 domain due to the growth of Ru NPs over the defects (see ESI†, Figure S3b and S4b).[20]

X-ray photoelectron spectroscopy (XPS) analysis was performed on both graphene supports (**G** and **P-G)** and obtained hybrid nanomaterials (**Ru/G** and **Ru/P-G**) to determine the chemical composition and the nature of the C, P and Ru species present (Figures 2 and S5). The C 1s signals of **G** and **P-G** appear as broad bands at binding energy (BE) of 284.5 eV, which can be deconvoluted in three components (see ESI†, Figure S5a-b). The main peak at 284.5 eV (orange) is assigned to the carbon atoms of graphitic layers (sp^2). The peak at *ca.* 286.4-286.2 eV (green) is attributed to carbon atoms bonded to P and those present in epoxides or tertiary alcohols. The last peak centred at ca. 288.9-288.6 eV (blue) corresponds to carboxylic groups.[21] Similarly, the P 2p signal of **P-G** is the result of the convolution of two components (see ESI†, Figure S5c), a major

This journal is © The Royal Society of Chemistry 20xx

Please do not adjust margins

Please do not adjust margins

peak at 132.9 eV corresponding to P atoms bonded to oxygen (blue curve), and a lower intensity one at 131.8 eV (green curve), for P-C bonds. These peaks were previously identified in similar P-doped graphenes[¡Error! Marcador no definido.] and fit well with the results obtained by FT-IR, where the characteristic P-O/P=O stretching band is observed at ca. 1160-1252 cm^{-1} for this support (see ESI†, Figure S6). In addition, the stretching vibration associated to aromatic C=C bonds from the graphene sheet appears at ca. 1600 cm^{-1}. Analysis of the P 2p signal allowed us to determine the P content in the doped support **P-G**, namely 1.15 at.%.

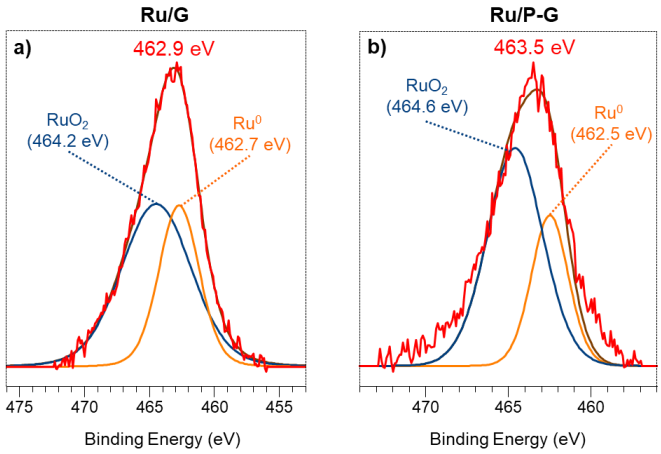

Figure 2. XPS signal of the Ru 3p band of as-synthesized **Ru/G** (a) and **Ru/P-G** (b).

Since the overlapping between the Ru 3d and C 1s signals makes difficult their deconvolution and interpretation, the different oxidation states of Ru in **Ru/P-G** and **Ru/G** were identified upon analysing the Ru 3p region. Figure 2a displays the Ru $3p_{3/2}$ signal of the as-synthesized **Ru/G**, at a BE of 462.9 eV. The deconvolution of this signal reveals two contributions, a major one at 464.2 eV, attributed to Ru^{IV} and characteristic of RuO_2, and a secondary one at 462.7 eV corresponding to Ru^0. The as-synthesized **Ru/G** surface approximately contains 64 % of Ru^{IV} and 36 % of Ru^0. Similarly, the Ru $3p_{3/2}$ signal of **Ru/P-G** (Figure 2b) presents a peak of BE at 463.5 eV, also containing two contributions, at 464.6 eV (RuO_2) and 462.5 eV (Ru^0). The surface of the as-synthesized **Ru/G** contains ca. 68 % of Ru(IV) and 32% of Ru^0.

^{31}P solid state NMR confirmed the presence of the dopant atoms in the P-doped graphene material and allowed to determine their chemical nature. ^{31}P MAS NMR spectra of both **P-G** and **Ru/P-G** display a broad peak between 10 and -40 ppm (see ESI†, Figure S7), as the result of the overlapped signals of phosphonate (7 to 10 ppm),[22] phosphate (ca. 0 ppm),[23] methaphosphate (-3 to -7 ppm),[¡Error! Marcador no definido.] elemental phosphorous (-14 to -17 ppm)[24] and/or polyphosphate (-22 ppm).[25] Elemental phosphorous comes from the reduction of the phosphate by carbon at high temperature during the pyrolysis of the P-doped graphene.[24] The presence of metaphosphate and polyphosphate groups could derive from the condensation of $H_2PO_4^-$ at 900 ºC.[¡Error! Marcador no definido.] Thus, most P-O bonds observed by XPS are due to phosphate-like structures.

Electrocatalytic performance in the HER.

The HER performance of **Ru/G** and **Ru/P-G** was evaluated in 1 M H_2SO_4 aqueous solution after their dispersion in THF (2 mg/mL) and drop-casting onto a glassy carbon rotating disk electrode (GC-RDE). A three-electrode configuration was used being the drop-casted GC-RDE the working electrode, SCE (saturated calomel electrode, KCl sat.) and a Pt wire the reference (RE) and counter (CE) electrodes, respectively. The polarization curves of **Ru/G** and **Ru/P-G** at t=0 s are shown in Figure 3 (bold lines). A change in the current density is observed when scanning towards reductive potentials, which is attributed to their catalytic activity to reduce protons to H_2.

The catalytic performance was significantly improved after a current-controlled bulk electrolysis at j = -10 mA/cm^2 (Figure 3a, dashed lines). As presented in Figure 3 and Table 1, whereas **Ru/G** and **Ru/P-G** show a η_{10} of 233 mV and 243 mV, respectively, a shift on the polarization curves is observed after the reductive process, improving the η_{10} to 29 mV and 15 mV, respectively. This behaviour is attributed to a change in the oxidation state of surface Ru atoms of the NPs: the partially oxidized surface of the as-synthesized NPs (see XPS analysis, Figure 2) is reduced to metallic Ru when submitted to a reductive treatment. The reduced species **Ru/G-r** and **Ru/P-G-r** are more active in HER than their as-synthesised counterparts **Ru/G** and **Ru/P-G**, displaying higher current densities and lower overpotentials. We previously reported a deep study of the proposed RuO_2/Ru interconversion with 4-phenylpyridne stabilized RuNPs,[5] confirming by XPS a total disappearance of the RuO_2 peak under reductive catalytic conditions.

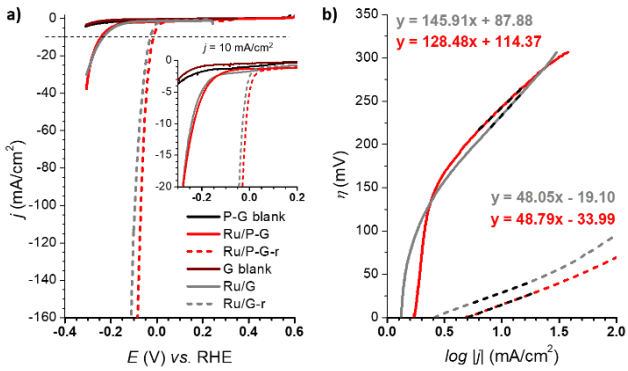

Figure 3. a) Polarization curves of **Ru/G** (grey line), **Ru/P-G** (red line) before (bold) and after (dashed) a reductive process at j = -10 mA/cm^2 in 1 M H_2SO_4. **G** (wine line), **P-G** (black line) blanks are also shown. b) Tafel plots of **Ru/G**, **Ru/G-r**, **Ru/P-G** and **Ru/P-G-r** in 1 M H_2SO_4. Same colour code as in (a).

The difference in nature and in catalytic performance between as-synthesised samples and their reduced analogous was also evidenced through the Tafel plots (Fig. 3b), obtaining improved overall kinetics with the reduced systems. The Tafel slope (b) allows defining the rate determining step (rds) of the catalytic reaction. Both **Ru/G** and **Ru/P-G** show a Tafel slope close to 120 mV, a consistent value with the Volmer step as rds (adsorption of H^+ to form the M-H species on the NPs, typically $b \approx 120$ mV/dec). In contrast, **Ru/G-r** and **Ru/P-G-r** show a Tafel slope of 48 mV/dec and 49 mV/dec, respectively, suggesting that the HER follows the Volmer-Heyrovsky mechanism with the Heyrovsky step (H_2 electro-desorption with a proton from the solution, $b \approx 40$ mV/dec) as the slowest path in the HER process.

Please do not adjust margins

Please do not adjust margins

The electrocatalytic performance of all the systems has been then compared by following the benchmarking methodology reported by Jaramillo *et al.*[26] First, the double-layer capacitance (C_{DL}) was estimated from the capacitive current in a non-Faradaic region using Eq. 1 shown below. Then, the electrochemically active surface area (ECSA) and roughness factor (RF) of all electrodes and supports were calculated from the obtained C_{DL} (see ESI†, Figures S8 and S9) according to equations 2 and 3.

$$i = vC_{DL} \qquad \textbf{Eq. 1}$$

$$\text{ECSA [cm}^2\text{]} = \frac{C_{DL}}{C_s} \qquad \textbf{Eq. 2}$$

$$\text{RF} = \frac{ECSA}{S} \qquad \textbf{Eq. 3}$$

The ECSA value allows calculating the specific current density (j_s) of the electrodes, which is the current density per "real" electroactive area at a given overpotential. Thus, the current density, j_s, normalized per ECSA at η= -100 mV, has been calculated for all the Ru materials before and after the reductive treatment/activation, as well as for the bare supports (*i.e.* **G** and **P-G**). The obtained results are summarized in Table 1. Regarding the bare supports, ECSA and RF data support the higher roughness of the non-doped support **G** (RF of 279.43 for **G** vs. 51.76 for **P-G**) already observed by TEM (see ESI†, Figure S1). Introduction of Ru NPs onto the carbon supports slightly increases the RF values in both cases (Table 1, entries 2 and 6). Activation of the hybrid electrodes **Ru/G** and **Ru/P-G** under reductive conditions (current-controlled bulk electrolysis at j = -10 mA/cm^2 for several hours) substantially increases the ECSA and RF values of both electrodes (compare entries 2 & 3 and 6 & 7). This increment may arise from surface changes in both the carbon supports and the Ru NPs (reduction process from Ru(IV) to Ru^0). The activated P-doped electrode, **Ru/P-G-r,** shows the highest HER activity among the tested electrodes, with a very low η_{10} of 15 mV, the highest exchange current density (j_0) and a specific current density 5 times higher than that of its non-doped counterpart **Ru/G-r**. For comparison purposes, the most relevant HER benchmarking parameters for the hybrid electrocatalysts developed in this work are collected in Table S1 (see ESI†) together with those of reported graphene-supported Ru-based systems and metal-free graphene-based materials. As can be inferred from the collected data, **Ru/G-r** and **Ru/P-G-r** show way higher HER performance than bare graphene-based electrodes and lay among the three state-of-the-art Ru-based systems.

Long-term stability is, together with kinetics, a key parameter for a catalyst to be potentially relevant in the HER. Thus, in a current controlled experiment (*i.e.* chronopotentiometry), **Ru/G-r** and **Ru/P-G-r** electrodes were hold at a constant current density of j = -10 mA/cm^2 for 12 h while monitoring the change in the required overpotential. Both systems showed almost no change for η_{10} and almost identical LSV polarization curves before and after 12h under catalytic turnover (Figure 4).

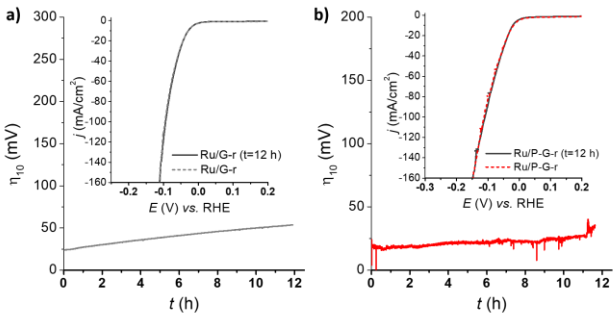

Figure 4. LSV of **Ru/G-r** (a) and **Ru/P-G-r** (b) before (dashed lines) and after (solid lines) a 12 h chronopotentiometry experiment at a j = -10 mA/cm^2.

Finally, a Faradaic efficiency of 97-98% was determined by quantifying the H_2 evolved by the systems during a 20 min chronoamperometry using a H_2-Clark electrode and comparing with the maximum theoretical amount of H_2 calculated from the total charge passed through each respective electrode (Figure 5). This result confirms the production of H_2 as the sole reaction taking place.

Table 1. Summary of physico-chemical and HER electrocatalytic data (1 M H_2SO_4) for the hybrid electrodes studied in this work.

Entry	Electrode	Ø (nm)	Ru (wt.%)	η_{10} (mV)	Tafel Slope (*b*) (mV/dec)	j_0 (mA/cm^2)	ECSA (cm^2)	RF	$\lvert j_s \rvert$ (η =100 mV) (mA/cm^2)
1	**G**						19.6	279.4	
2	**Ru/G**	1.9 ± 0.6	2.6	233	146	0.25	27.6	393.9	0.005
3	**Ru/G-r**	-	-	29	48	2.50	41.9	598.9	0.184
4	**P-G**						3.6	51.8	
5	**P-G-r**						10.4	147.9	
6	**Ru/P-G**	1.5 ± 0.3	3.3	243	128	0.13	4.6	66.1	0.032
7	**Ru/P-G-r**	-	-	15	49	4.97	21.4	305.1	0.883

This journal is © The Royal Society of Chemistry 20xx

Please do not adjust margins

Please do not adjust margins

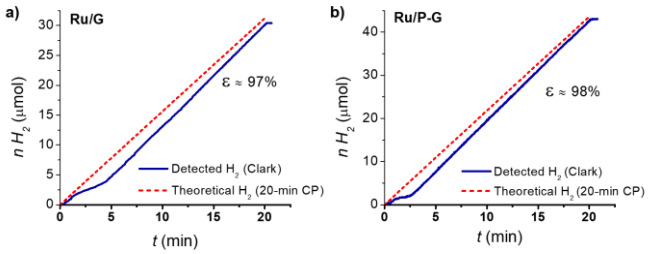

Figure 5. H_2-monitored current-controlled bulk electrolysis of **Ru/G** (a) and **Ru/P-G** (b) in 1 M H_2SO_4. The produced H_2 was quantified in the gas phase using a Clark-type electrode.

The fate of the hybrid electrodes under turnover conditions has been studied by TEM after performing a 2h CP to each system (j = -10 mA/cm^2). Each material was recovered from the electrode by sonication in THF and drop-casted onto a TEM grid. Interestingly, the presence of small NPs onto the graphene supports is still visible (see ESI†, Figures S10 and S11). Moreover, the reductive potential applied for 2 h did not change significantly the size and morphology of the Ru NPs. In order to verify the nature of the NPs on-top of the graphene supports, EDX analysis of **Ru/P-G** has been performed after 2 h under catalytic conditions (see ESI†, Figure S12). The results confirm the presence of Ru in the sample, therefore corroborating the TEM data, and highlight the stability of the supported Ru NPs after short-term catalytic turnover.

Conclusions

Bare and P-doped graphenes arising from the pyrolysis of biomass (alginate from marine algae) were used as a support for the growth and stabilization of ultra-small Ru/RuO_2 NPs through organometallic synthesis. Compared to bare counterpart, P-doped graphene allowed obtaining smaller and better dispersed NPs in hybrid electrodes of lower roughness and electroactive surface area. Electrochemical activation of the supported nanocatalysts by reduction of the passivating RuO_2 layer, offers excellent HER electrocatalysts under acidic conditions (η_{10} of 29 mV and 15 mV for the bare and P-doped electrodes, respectively). P doping, identified as surface phosphates by ^{31}P solid state NMR, induces a general improvement of all HER benchmarking parameters determined, including overpotential (η_{10}) and exchange (j_0) and specific (j_s) current densities. All studied systems show excellent long-term stability and selectivity for hydrogen generation with no sign of deactivation after 12 h under turnover conditions and quasi quantitative Faradaic efficiencies. Altogether, this work evidences how the combination of an efficient nanocatalyst synthesis method with the doping of graphene supports provides performant hybrid electrodes for the production of hydrogen.

Experimental Section

General procedures and starting materials

Most of chemical operations were carried out using standard Schlenk tubes, Fischer–Porter bottle techniques under nitrogen atmosphere or in a glovebox under nitrogen atmosphere. Tetrahydrofuran (THF) was purified before use by distillation under argon atmosphere through filtration in the column of a solvent purification system (SPS). The organometallic precursor, [Ru(COD)(COT)], was purchased from Nanomeps (Toulouse), and alginic acid sodium salt and sodium phosphate dibasic from Sigma Aldrich. All reagents were used without purification.

Transmission electron microscopy (TEM) and high-resolution TEM (HRTEM). TEM and HRTEM images were performed at the "Servicio de Microscopía Electrónica" of Universitat Politècnica de València (UPV) by using a JEOL JEM 1400 Flash electron microscope operating at 120 kV with a point resolution of 3.8 Å and a JEOL JEM 2010 electron microscope working at 200 kV with a resolution point of 2.35 Å, respectively. The average particle size for both supported-Ru NPs was obtained by measuring more than 100 particles of each material by using the ImageJ software. FFT treatments have been carried out with Digital Micrograph.

Elemental Analysis (EA). EA analyses of nitrogen, carbon and hydrogen were determined with a Euro EA3000 Elemental Analyzer (EuroVector) using sulfanilamide as reference.

Inductively coupled plasma atomic emission spectroscopy (ICP-AES). ICP-AES analyses of **Ru/G** and **Ru/P-G** were carried out at the ITQ by using a Varian 715-ES ICP-Optical Emission Spectrometer, in order to determine the Ru content. The samples for ICP were prepared following a modified digestion method previously reported.[27] A small portion of the material (30 mg) was suspended in 21 mL HCl-HNO_3 (6:1) and then, the solution was sonicated for 90 minutes. Then, the samples were digested at 180 °C for 15. Finally, they were cooled down until room temperature, diluted with 100 mL of water and afterwards analyzed by ICP-AES.

Solid-state MAS-NMR spectroscopy. ^{31}P analyses were performed at the ITQ on a Bruker Avance 400WB instrument equipped with a 4 mm probe with a sample rotation frequency of 10 kHz. Measurements were carried out in a 4 mm ZrO_2 rotor.

Please do not adjust margins

Please do not adjust margins

Raman Spectroscopy. Raman spectra were recorded with a 514 nm laser excitation in a Renishaw in via Raman spectrometer equipped with a Lyca microscope. The samples (powder) were deposited on an Al support and measured in the region between 0 and 3000 cm^{-1} with a resolution of < 4 cm^{-1}.

X-ray photoelectron spectroscopy (XPS). XPS analyses were recorded using a SPECS spectrometer equipped with a Phoibos 150MCD-9 multichannel detector using Mg-Kα (1235.6 eV) and Al-Kα (1483.6 eV) irradiation from a dual source. The pressure during the measurements was kept under 10^{-9} Torr. The quantification and titration of the spectra were performed with the help of the CASA software, referencing them to the C1s peak (284.5 eV).

Infrared spectroscopy (IR). FT-IR spectra were recorded on a Nicolet 8700 Thermo spectrometer in the range 4000-600 cm^{-1} from samples prepared as KBr pellets.

X-ray Powder Diffraction (XRD). Powder samples were analysed using a CUBIX PANalytical diffractometer equipped with a PANalytical X´Celerator detector. X-ray monocromatic radiation of CuKα (λ_1=1.5406 Å, λ_2=1.5444 Å, I_2/I=0.5) was employed.

Synthesis of graphenes

G. G was synthesized by pyrolysis of alginate according to previous literature.[¡Error! Marcador no definido.,¡Error! Marcador no definido.] In particular, the alginic acid sodium salt was pyrolized at 900 °C for 2 h (rate of 10 °C/min) under Ar atmosphere. The resulting graphitic powder was sonicated during 1 hour in water to obtain the G support.

P-G. P-G was synthesized by pyrolysis of alginate according to previous literature,[¡Error! Marcador no definido.,23] dissolving 0.5 g of alginic acid sodium salt in a sodium phosphate dibasic monohydrate aqueous solution (1.6 g in 50 mL of water). After that, the resulting black powder was pyrolized in the same way as G support.
EA: C=73.54%, H: 0.96%, S: 0.331%
XPS: P=1.15 %
XRD: Reduced graphene oxide
IR: (KBr pellet, cm^{-1}), 1160 cm^{-1} (ν P=O).

Synthesis of graphene-supported Ru NPs

Ru/G and Ru/P-G*: In a Schlenk tube,* 10 mg (0.032 mmol) of [Ru(COD)(COT)] were dissolved in 5 mL THF (previously deoxygenated). At the same time, a Fischer-Porter bottle was charged with **G** or **P-G** (100 mg) and dispersed in 50 mL of deoxygenated and anhydrous THF by ultrasonication (90 min). Then, the [Ru(COD)(COT)] solution was transferred to the Fischer-Porter bottle and it was pressurized with 3 bar of H_2. After 20 h under vigorous stirring at room temperature, the pressure was released and **Ru/G** or **Ru/P-G** were separated from the suspension in the fume hood by filtration through a polyamide membrane (Whatman® membrane filters, 47mm×0.45 µm) and washed with THF (100 mL). The resulting black precipitates were dried overnight at 60 °C. The size of the NPs was measured by TEM on a population of at least 100 NPs, affording a Ru NP mean diameter of 1.9 (0.6) nm and 1.5 (0.3) nm for **Ru/G** or **Ru/P-G**, respectively. Ru contents (ICP-AES): 2.6 % and 3.3 % for **Ru/G** or **Ru/P-G**, respectively.

Electrochemical measurements: All the electrochemical experiments were performed with a BioLogic SP-150 potentiostat. The solutions were degassed previous to the electrochemical analysis with an Ar flow. Ohmic potential (IR) drop was automatically corrected at 85 % using the Biologic EC-Lab software for linear sweep voltammetry. 1 M H_2SO_4 solution was prepared by mixing 56.1 mL of 95-97 % H_2SO_4 in 1 L of Milli-Q water. A glassy carbon rotating disk electrode (RDE, ϕ = 0.3 cm, S = 0.07 cm^2) was used as working electrode. The electrode preparation started from a 2 mg/mL dispersion of each material by adding 1 mg of Ru material in 0.5 mL of THF. Long-time sonication was applied to prevent NP aggregation over the C support. Then, an aliquot of 5 µL was drop-casted on the surface of the GC/RDE (S = 0.07 cm^2), and dried. A 5 µL-drop of Nafion (0.02% w/w in water and 1-metanol) was finally added and dried prior to the electrochemical measurements. The RDE was rotated at 3000 rpm in order to ensure complete removal of *in situ* formed H_2 bubbles during catalytic turnover. A Pt wire was used as counter electrode (CE) and a standard calomel electrode (SCE, Hg/Hg_2Cl_2, KCl sat.) was used as a reference electrode (RE). The potentials reported versus normal hydrogen electrode were transformed as follows ($E_{NHE} = E_{SCE} + E^0_{SCE}$), where E^0_{SCE} = 0.244 V.
A 10 mL two-compartment cell with a proton exchange membrane between the two compartments was used for faradaic efficiencies calculation. The CE was placed in one compartment and the WE and RE were placed in the other one together with the Clark electrode. Both compartments were filled with *c.a.* 7 mL of 1 M H_2SO_4 solution and equipped with a stirring bar. Prior to each measurement, both compartments were purged with Ar. Unisense H_2-NP Clark electrode was used to measure the hydrogen evolved in the gas phase during a chronopotentiometry. The Clark electrode was calibrated by adding different volumes of 99 % pure hydrogen at the end of the experiment.
Double-layer capacitance (C_{DL}) and electrochemically active surface area (ECSA) determination: C_{DL} was estimated by performing CV measurements with different scan rates. A non-faradaic region was chosen from the LSV (typically a 0.1 V window about OCP), where no redox process takes place and all the measured current is due to double-layer charging. Based on this assumption, the charging current (i_c) can be calculated as the product of the electrochemical double-layer capacitance (CDL) by the scan rate (ν). Plotting i_c as a function of ν yields a straight line with slope equal to C_{DL}. In this way, 8 different scan rates were used (5, 10, 25, 50, 75, 100, 250 and 500 mV/s), holding the working electrode at each potential vertex for 10 seconds prior to the next step. The ECSA was obtained by dividing the calculated capacitance by a tabulated value (C_S = specific capacitance) that depends on the material used and solution (for C, in 1 M H_2SO_4 C_S=13-17 µF/cm^2). The roughness

This journal is © The Royal Society of Chemistry 20xx

Please do not adjust margins

Please do not adjust margins

factor (RF) was calculated by dividing the ECSA by the geometrical surface area (S) of the RDE.

Author Contributions

L.M. performed the electrochemical experiments and characterization of the electrodes after catalysis and participated in writing – review and editing. C. C-N. and M.P. performed the synthesis and structural/spectroscopic characterization of the hybrid electrodes. N.R. coordinated the tasks between researchers and participated in writing – review and editing. R.B., K.P., J.G-A and A.C supervised the project and participated in writing – review and editing. X.S. and LM.M-P. conceived the idea of the project and wrote the original draft with input from other authors. All authors contributed to the design of experiments, analysis of the results and preparation of the manuscript.

Conflicts of interest

There are no conflicts to declare.

Acknowledgements

The authors thank Instituto de Tecnología Química (ITQ), Consejo Superior de Investigaciones Científicas (CSIC), Universitat Politècnica de València (UPV), Universitat Autonoma de Barcelona for the facilities. Electron Microscopy Service of the UPV for TEM facilities and Jose A. Vidal-Moya (ITQ, CSIC-UPV) for NMR measurements are also thanked. C. C.-N. gratefully acknowledges Generalitat Valenciana predoctoral fellowship (GVA: ACIF/2019/076) and L. M. P the UAB for a PhD grant. This work was financially supported by the MINECO/FEDER project PID2019-104171RB-I00. J. G.-A. acknowledges the Serra Húnter Program. CNRS and Université de Toulouse-Paul Sabatier are also acknowledged.

References

[1] Intergovernmental Panel on Climate Change. *Global Warming of 1.5 °C* (IPCC, 2018).
[2] M. A. Rosen, S. Koohi-Fayegh, *Energ. Ecol. Environ*. 2016, **1**, 10-29.
[3] C. Amiens, D. Ciuculescu-Pradines, K. Philippot, *Coord. Chem. Rev.* 2016, **308**, 409–432.
[4] L. M. Martínez-Prieto, B. Chaudret, *Acc. Chem. Res.* 2018, **51**, 376-384.
[5] J. Creus, S Drouet, S. Suriñach, P. Lecante, R. Poteau, K. Philippot, J. García-Antón, X. Sala, *ACS Catal.* 2018, **8**, 11094-11102.
[6] J. Creus, J. De Tovar, N. Romero, J. García-Antón, K. Philippot, R. Bofill, X. Sala, *ChemSusChem* 2019, **12**, 2493-2514.
[7] N. Romero, R. Barrach, L. Gil, S. Drouet, I. Salmeron-Sànchez, O. Illa, K. Philippot, M. Natali, J. García-Antón, X. Sala, *Sust. Energ. & Fuels* 2020, **4**, 4170-4178.
[8] L. Mallón, N. Romero, A. Giménez, E. M. Morales, J. Alemán, R. Más-Ballesté, R. Bofill, K. Philippot, J. García-Antón, X. Sala, *Catal. Sci. Technol.* 2020, **10**, 4513-4521.
[9] J. De Tovar, N. Romero, S. Denisov, R. Bofill, C. Gimbert-Suriñach, D. Ciuculescu-Pradines, S. Drouet, A. Llobet, P. Lecante, Z. Freixa, N. McClenaghan, C. Amiens, J. García-Antón, K. Philippot, X. Sala *Mater. Today Energ.* 2018, **9**, 506-515.
[10] J. Zhang, Z. Xia, L. Dai, *Sci. Adv.* 2015, **1**, e1500564.
[11] A. Bähr, G.-H. Moon, H. Tüysüz, *ACS Appl. Energy Mater.* 2019, **2**, 6672-6680.
[12] L. Wang, Z. Sofer, M. Pumera, *ACS Nano* 2020, **14**, 21-52.
[13] A. Ambrosi, C. K. Chua, A. Bonanni, M. Pumera, *Chem. Rev.* 2014, **114**, 7150-7188.
[14] D. D. Ouyang, L. B. Hu, G. Wang, B. Dai, F. Yu, L. L. Zhang, *New Carbon Mater.* 2021, **36**, 350-372.
[15] M. Latorre-Sánchez, A. Primo, H. García, *Angew. Chem. Int. Ed.* 2013, **52**, 11813-11816.
[16] M.-M. Trandafir, M. Florea, F. Neaţu, A. Primo, V. I. Parvulescu, H. García, *ChemSusChem*, 2016, **9**, 1565-1569.
[17] L. M. Martínez-Prieto, M. Puche, C. Cerezo-Navarrete, B. Chaudret, *J. Catal.* 2019, **377**, 429-437.
[18] C. Cerezo-Navarrete, Y. Mathieu, M. Puche, C. Morales, P. Concepción, L. M. Martínez-Prieto, A. Corma, *Catal. Sci. Tech.* 2021, **11**, 494-505.
[19] S. Navalon, A. Dhakshinamoorthy, M. Alvaro, H. Garcia, *Coord. Chem. Rev.*, 2016, **312**, 99-148.

Please do not adjust margins

Please do not adjust margins

[20] S. Stankovich, D. A. Dikin, R. D. Piner, K. A. Kohlhaas, A. Kleinhammes, Y. Jia, Y. Wu, S. T. Nguyen, R. S. Ruoff, *Carbon* 2007, **45**, 1558-1565.
[21] Graphene Oxide: Fundamentals and Applications, First Edition. Eds: A. M. Dimiev; S. Eigler. 2017 John Wiley & Sons, Ltd. Published 2017 by John Wiley & Sons, Ltd.
[22] A. M. Puziy, O. I. Poddubnaya, R. P. Socha, J. Gurgul, M. Wisniewski, *Carbon*, 2008, **46**, 2113-2123.
[23] M. J. McAllister, J.-L. Li, D. H. Adamson, H. C. Schniepp, A. A. Abdala, J. Liu, M. Herrera-Alonso, D. L. Milius, R. Car, R. K. Prud'homme, I. A. Aksay, *Chem. Mater.* 2007, **19**, 4396-4404.
[24] R. Fu, L. Liu, W. Huang, P. Sun, *J. App. Polymer Sci.* 2003, **87**, 2253-2261.
[25] M. Hupfer, B. Ruübe, P. Schmieder, *Limnol. Oceanogr.* 2004, **49**, 1-10.
[26] C. C. L. McCrory, S. Jung, I. M. Ferrer, S. M. Chatman, J. C. Peters, T. F. Jaramillo, *J. Am. Chem. Soc.* 2015, **137**, 4347-4357.
[27] T. Suoranta, M. Niemelä, P. Perämäki, *Talanta* 2014, **119,** 425-429.

This journal is © The Royal Society of Chemistry 20xx

Please do not adjust margins